JOURNAL OF AIRCRAFT
Vol. 44, No. 4, July–August 2007

Experimental Investigation of Unsteady Flow Separation on a Maneuvering Axisymmetric Body

Serhat Hosder* and Roger L. Simpson†
Virginia Polytechnic Institute and State University, Blacksburg, Virginia 24061

DOI: 10.2514/1.26804

An experimental study on maneuvering-undersea-vehicle geometry was conducted to give detailed information on unsteady turbulent flow separation and to investigate different time-lag models for approximating the unsteady separation locations. Both unsteady and steady results are presented for the axisymmetric configuration of the model, which can also be thought of as a missile or aircraft-fuselage geometry. Steady and unsteady skin-friction magnitudes were measured using hot-film sensors. The minimum of the circumferential skin-friction distribution at each axial-measurement station was used to detect the separation locations. The linear pitch-up maneuver studied is comparable to the dynamic motion of full-scale vehicles of interest, in terms of the nondimensional time. Significant time lags observed between unsteady and steady crossflow separation locations indicate the increase in attached circulation over the maneuvering model, which may explain why unsteady forces measured on similar geometries lead the steady values. A first-order differential time-lag model approximates the unsteady separation locations reasonably well. This model can be considered as a method of correlating the unsteady measurements to the quasi-steady data with a time lag. Using this model, the prediction of the unsteady flow characteristics from the steady data can be possible with the development of methods for estimating the time lags that vary based on the geometry and the maneuvers performed. The results of the unsteady experiments presented in this paper show that the time required to displace the volume of leeside inviscid fluid during a maneuver with vortical separated flow may be the main factor creating the difference in the time-lag magnitudes and their spatial variation observed for different axisymmetric geometries and points of rotation.

Nomenclature

A, B	=	hot-film-sensor calibration coefficients
a	=	model radius of the constant-diameter region
C_f	=	skin-friction coefficient
C_p	=	pressure coefficient
E	=	time-averaged voltage value
F	=	generalized steady and quasi-steady aerodynamic vector function
G	=	generalized unsteady aerodynamic vector function
H	=	shape factor
$\bar{h}$	=	mean heat-transfer film coefficient
L	=	model length
Re_a	=	radius-based Reynolds number, $U_\infty a/\nu$
Re_L	=	length-based Reynolds number, $U_\infty L/\nu$
Re_θ	=	momentum-thickness-based Reynolds number, $U_\infty \theta/\nu$
T_w	=	hot-film-sensor temperature
T_∞	=	freestream temperature
t_{ref}	=	reference time, L/U_∞
t'	=	nondimensional time, tU_∞/L
U_e	=	boundary-layer-edge velocity
U_∞	=	freestream velocity
x	=	model longitudinal position from the nose
x_{cg}	=	location of the center of rotation
z	=	plunge ordinate of dynamic plunge-pitch-roll model mount
α	=	angle of attack measured at the model center of rotation and pitch angle of dynamic plunge-pitch-roll model mount
α_{eff}	=	effective angle of attack, $\alpha_{\text{eff}} = \alpha - \Delta\alpha_{\text{eff}}$
$\dot{\alpha}$	=	dimensional pitch rate
β	=	sideslip angle
$\Delta\alpha_{\text{eff}}$	=	incremental effective angle of attack
δ	=	boundary-layer thickness
δ^*	=	displacement thickness
θ	=	momentum thickness
ν	=	kinematic viscosity
τ_w	=	wall shear stress
τ'	=	first-order time lag in nondimensional units
ϕ	=	circumferential location on the model surface measured from the windward line of symmetry
ϕ_{sep}	=	separation location
ϕ_{uns}	=	approximation to the unsteady separation location
ϕ_0	=	quasi-steady separation location

Received 27 July 2006; revision received 15 December 2006; accepted for publication 18 December 2006.

*Postdoctoral Associate, Department of Aerospace and Ocean Engineering. Member AIAA.
†Jack E. Cowling Professor, Department of Aerospace and Ocean Engineering, Fellow AIAA.

I. Introduction

THE study of truly unsteady, high-excursion, and high Reynolds number separated flows over undersea vehicles, aircraft, or missiles has become of great importance in the analysis and the improvement of the dynamic performance. Because of their highly complex, three-dimensional, turbulent and separated nature, standard stability-derivative techniques fail to capture the nonlinearities in these flows, and computational fluid dynamics (CFD) techniques need physical models that can resolve the complexities of such flowfields to get accurate and more reliable results. Suitable simulations of the maneuvers in the wind tunnels are not only important for understanding the physics of complex flow phenomena, but also supply the necessary information required for the development and the validation of physics-based models used in CFD. The dynamic plunge-pitch-roll (DyPPiR) model mount, a computer-controlled, three-degree-of-freedom robotic arm at the Stability Wind Tunnel of Virginia Polytechnic Institute and State University (Virginia Tech), provides the unique capability of performing general preprogrammed, high-excursion, large-scale, high Reynolds number maneuvers [1,2].

Dynamic testing has been an important part of design and validation of various types of craft for decades. Generally, these

techniques are quasi-steady and can describe small-excursion maneuvers reasonably well [3]. As discussed by Wetzel and Simpson [4], there is a significant difference between quasi-steady and unsteady aerodynamics. In a quasi-steady approach, the aerodynamics of a maneuvering body are dependent only on the instantaneous state of the model (angle of attack, sideslip angle, control-surface deflections, etc.), whereas in fully general unsteady aerodynamics, time-history effects on the state variables are also included. Mathematically, the distinction between quasi-steady and unsteady aerodynamics can be shown as follows: steady, $\boldsymbol{F}(\alpha, \beta, \ldots)$; quasi steady, $\boldsymbol{F}[\alpha(\boldsymbol{t}'), \beta(\boldsymbol{t}'), \ldots]$; and fully unsteady $\boldsymbol{G}[\boldsymbol{t}', \alpha(\boldsymbol{t}'), \dot{\alpha}(\boldsymbol{t}'), \beta(\boldsymbol{t}'), \dot{\beta}(\boldsymbol{t}'), \ldots]$, where $\boldsymbol{F}$ and $\boldsymbol{G}$ can be a dominant flow feature such as separation location. Here, the nondimensional time is given by Etkin [5]:

$$\boldsymbol{t}' = \frac{t}{t_{\text{ref}}} = \frac{tU_\infty}{L} \tag{1}$$

In the preceding equation, t_{ref} represents the time for the flow to pass over a model: L/U_∞. The history effects mainly cause time lags or leads between the unsteady and the corresponding instantaneous quasi-steady flowfields, which can be quantified by measuring flow separation locations or the aerodynamic loads on a body undergoing maneuvers.

The objectives of the current experimental study are to

1) Give detailed information on unsteady turbulent flow separation over a maneuvering axisymmetric model.

2) Explain the difference between the steady and unsteady separation structure over the same geometry.

3) Investigate algebraic and first-order differential time-lag models to approximate the unsteady flow separation locations.

To achieve these objectives, hot-film sensors were used in the experiments to measure the skin-friction magnitudes over the model surface. The unsteady results of the current study will show that the main flow topology over the axisymmetric model is dominated with unsteady crossflow separation, which creates time lags between the steady and unsteady separation locations. The main interest is to be able to develop physics-based models to approximate these time lags, which requires the experimental data obtained from realistic simulations of the dynamic phenomenon.

As shown by Wetzel et. al. [6], the local minimum of the skin friction in the circumferential direction of an axisymmetric body is a good indicator of crossflow separation. Following the results of that work, the separation location is defined to be the local minimum of the skin friction in this study. In the experiments, steady skin-friction measurements were obtained at different angles of attack, and the unsteady maneuver studied is a dynamic ramp pitch-up motion simulated by the DyPPiR. This maneuver is comparable to full-scale undersea-vehicle dynamic motions, in terms of the nondimensional time t', and was selected to create a strong unsteady turbulent flow separation on the model. It should also be noted that this type of maneuver is common for most high-performance aircraft, rockets, and missiles. Therefore, the study of unsteady flow characteristics under such maneuvers plays an important role for understanding and improvement of the dynamic performance.

The model used in the experiments was designed in an effort to obtain code-validation data on a submarine-type vehicle, as described by Groves et. al. [7], and has an axisymmetric hull geometry that can be used with or without typical appendage components such as a sail and four identical stern appendages. The model and the subsequent experimental project were referred to as SUBOFF by the same group and will be referenced the same way in this paper. In the main part of this paper, both steady and unsteady results are presented for the bare-body (axisymmetric) configuration of the model. The bare body can also be thought of as a missile or, to a certain extent, an aircraft-fuselage geometry, which makes the results of this study applicable to the aerodynamic analysis of a wide range of practical aerospace applications undergoing different maneuvers. In addition to the bare-body results, the observations from the steady skin-friction measurements over the sail-on-side model are given in Appendix B to show the change in the separation structure.

Among the previous studies, the unsteady-crossflow-separation-location measurements on a maneuvering 6:1 prolate-spheroid model by Wetzel and Simpson [3] can be considered as the most similar work to that presented here, in terms of the experimental measurement technique and the unsteady high-excursion maneuver performed. In that work, significant time lags were detected between unsteady and steady flow separation on the prolate spheroid undergoing pitch-up and turning maneuvers. Wetzel and Simpson [4] also found that a first-order differential lag model fits the unsteady data reasonably well. Recent studies performed by Granlund and Simpson [8] included unsteady force and moment data on a maneuvering undersea vehicle. In their work, the force and moment data were obtained by using custom-designed load cells for the same geometry used in the skin-friction measurements described in this paper. The maneuver was also the same as that performed for the current work. A review of some other relevant studies of three-dimensional unsteady aerodynamic experiments on various bodies was given by Wetzel and Simpson [4] and Hosder [9].

II. Experimental Apparatus and Techniques

A. Wind Tunnel and the DyPPiR

The experiments were conducted in the Virginia Tech Stability Wind Tunnel, a closed-return subsonic facility powered by a 450-kW dc motor driving a 4.27-m-long propeller. The tunnel has a 1.8×1.8 m square test section and a maximum speed of 80 m/s, with a very low freestream turbulence level of 0.03% [1]. A slotted-wall test section with a 38% open-area ratio was used in the experiments to reduce model-blockage effects. The dynamic plunge, pitch, and roll actuator installed in the Virginia Tech Stability Wind Tunnel (Fig. 1) is a computer-controlled model mount with three degrees of freedom: plunge with a vertical range of 1.5 m from the tunnel centerline, pitch with a range of ± 45 deg, and roll with a range of ± 360 deg. The three hydraulic actuators enable the DyPPiR to carry a maximum model load of 45 and 250 kg of hardware at rates approaching 9 m/s in plunge and 120 deg/s in pitch. By the combined motion of pitch and plunge actuators, the DyPPiR can perform maneuvers around an arbitrary center of rotation, which is important for obtaining the correct lateral velocities across the aircraft and the submarines. These unique features of the DyPPiR allow one to simulate the preprogrammed, general, high-excursion, rapid maneuvers and to keep the model in the desired location and orientation in steady testing. The coordinate nomenclature for the DyPPiR and the model is given in Fig. 2. Note that the circumferential location ϕ is measured from the windward line of symmetry in the counterclockwise direction.

B. Wind-Tunnel Model

The lightweight SUBOFF model has a generic undersea-vehicle geometry [7] with a scaled length L of 2.24 m. The model has a bow

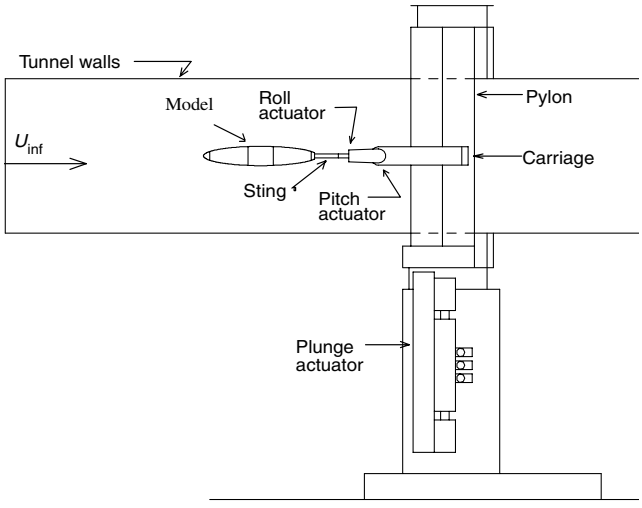

Fig. 1 DyPPiR model mount installed in the wind tunnel [3].

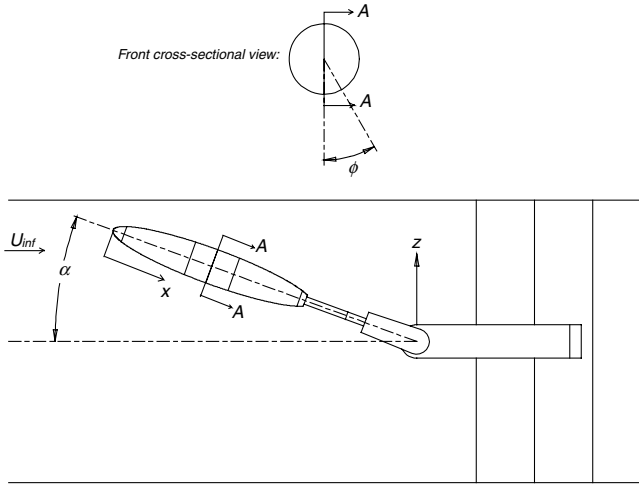

Fig. 2 Coordinate nomenclature for DyPPIR [3].

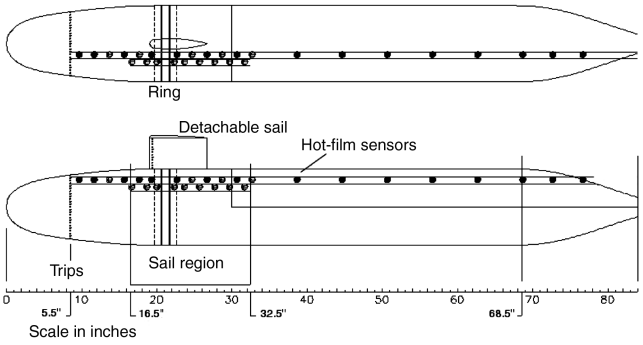

Fig. 3 Top and side views of the model and hot-film-sensor locations.

region for $0.0 \leq (x/L) \leq 0.23$, a constant-diameter region for $0.23 \leq (x/L) \leq 0.75$, and an afterbody (stern) region for $0.75 \leq (x/L) \leq 1.0$. The construction of the model was highly accurate and the built-model tolerances were within 0.25 mm. Because of high stiffness and light weight, the deformation of the composite model and the support under steady and dynamic loads was negligible. A detailed description of the model construction is given by Whitfield [10]. Figure 3 shows the model geometry with the hot-film-sensor locations. For the experiments, the last 0.2 m of the stern region of the original SUBOFF geometry was removed to make the model support fit inside the model. The sail can be detached, resulting in the axisymmetric configuration of the model. The bare-body measurements were performed by using 15 sensors located at certain positions of the long row (Fig. 3).

To fix the transition location on the model and further guarantee a Reynolds-number-insensitive separation, trip posts of 0.76-mm-high cylinders with 1.28-mm diameter, spaced 2.5 mm apart, were placed on the model nose at $x/L = 0.10$. Two rows of the same trip posts were put on the lower and the upper surfaces of the sail in the spanwise direction. The rows were located 0.64 cm (measured on the surface) away from the leading edge of the sail. The same trip location was used by Whitfield [10] for the same geometry and the flow conditions in unsteady force and moment measurements. The effect and the selection of the specific trip location for the current model was studied in detail by Wetzel and Simpson [11].

C. Hot-Film Sensors

To measure the skin friction, hot-film sensors designed and documented by Simpson et al. [12] were used. The sensors are made of Balco foil (70% nickel and 30% iron) and the main sensing area is a spiral of 5.1 mm in diameter. These directionally insensitive hot-film sensors were designed to measure the magnitude of the skin friction [12]. The sensors heat the near-wall fluid by forced convection. Because of the similarity between the gradient transport of momentum and scalars (heat), heat transfer in the fluid gives a measure of the wall shear. The mean film coefficient $\bar{h}$ is proportional to the cube root of the near-wall velocity gradient, which is thus proportional to the wall shear τ_w. Hot-film sensors were operated with Miller-type nonlinearized constant-temperature anemometers [13]. The same sensor-anemometer setup was used in a prolate-spheroid study by Wetzel and Simpson [3], who reported a flat frequency response up to roughly 200 Hz. Because of relatively low frequency response and large sensor size (diameter of 5.1 mm), the sensors are insensitive to high-frequency, small-scale, turbulent fluctuations. However, the frequency response is high enough to resolve the time history of the spatially averaged skin-friction values in maneuvers. A detailed explanation of the hot-film-sensor-calibration procedure is given in Appendix A.

D. Description of Steady Measurements and Dynamic Maneuvers

All skin-friction measurements were done with a tunnel speed of $42.7 \pm 1\%$ m/s. For these experiments, the Reynolds number based on the modified model length (Re_L) was 5.5×10^6. The oil-flow visualizations were taken at a Reynolds number of $Re_L = 4.5 \times 10^6$. Ahn [14] showed that there exists a critical Reynolds number of 2.5×10^6 for the flow past a 6:1 prolate spheroid at different angles of attack. Above this critical value, as the Reynolds number increases, the crossflow separation is fully turbulent and the separation lines do not change their circumferential location, but stretch to the upstream of the body. Because the Reynolds numbers used in hot-film measurements and the oil-flow visualizations of the case discussed in this paper are both well above the critical value, quantitative data from the hot-film measurements and the qualitative observations from the oil-flow visualizations should supply information for the same flow pattern and the separation structure.

Steady hot-film measurements were taken at 14 angles of attack, starting from 0.9 deg. The last angle covered was 27.6 deg. The difference between each steady angle of attack ranged from 1.9 to 2.2 deg. These angles are shown by solid square symbols in Fig. 4. In addition to obtaining the steady surface flow structure over the model, the results of the steady data at these angles of attack were also used to construct the quasi-steady data to be used in a first-order differential time-lag model, which will be described in Sec. III.

Unsteady results were obtained for the pitch-up maneuver. The pitch-up maneuver performed for the present work is a simple linear ramp from 1 to 27 deg in 0.33 s. Figure 4 shows the DyPPiR pitch angle and plunge location for the pitch-up maneuver. The uncertainty in plunge location is ± 0.003 m at the 95% confidence interval and the uncertainty for the pitch angle is ± 0.2 deg at the same confidence level. The DyPPiR pitch angle is also the instantaneous angle attack measured at the model center of rotation. Note that the actual maneuver starts at $t' = 3.00$. The maneuver was performed with a constant pitch rate of 78 deg/s and the model center of rotation was at $x_{cg}/L = 0.24$. For each ϕ orientation of the model, the pitch-up

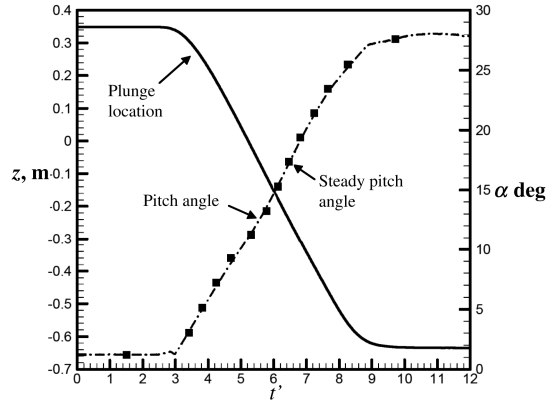

Fig. 4 DyPPiR plunge location and pitch angle for the pitch-up maneuver; filled symbols show the pitch angle values for the steady measurements.

maneuver was executed 10 times. Unsteady skin-friction values at each x/L measurement station were calculated for each repetition and the final values were obtained by ensemble averaging. Further details about the unsteady data reduction may be found in [9].

Measurements of the skin friction in steady experiments and unsteady tests were performed for two model configurations: bare-body and sail-on-side cases. In the bare-body case, both steady and unsteady skin-friction data were acquired between $\phi = 0$ and 180 deg in the circumferential direction, with 10-deg increments on the windward side and for every 2 deg on the leeward side. For the sail-on-side case, measurements were made between $\phi = 0$ and 360 deg. The increment was again 2 deg on the leeward side to locate the crossflow separation locations with low uncertainty. On the windward side, measurements were made with 10-deg increments, except the region between $\phi = 270$ and 292 deg, in which the skin friction was measured every 2 deg to resolve the surface flow structure in the vicinity of the sail. In this paper, we focus on the steady and the unsteady measurements over the bare body, because the results obtained for this configuration of the model can be applied to many aerospace geometries of interest. In Appendix B, a detailed discussion of steady results obtained with the sail-on-side configuration is presented.

E. Uncertainties in Measured Quantities

The steady skin-friction magnitudes have an uncertainty of $\pm 6\%$ for random uncertainties at the 95% confidence level. For the unsteady skin-friction magnitudes, uncertainty is $\pm 8\%$ at the same confidence level. The uncertainty in the determination of the separation locations is ± 2 deg. The details of the uncertainty calculation can be found in [9].

III. Results and Discussion

A. Steady Results

Before the discussion of the unsteady flow separation, it is essential to summarize some steady results to understand both the qualitative and the quantitative differences between the unsteady and the steady crossflow separation. In addition, a first-order differential time-lag model to be used later in this paper requires the quasi-steady separation information, which is constructed from the steady data. The following subsection gives an overview of the steady skin-friction measurements. The steady pressure information obtained at two angles of attack are also presented to show that the pressure data may not be an accurate measure of crossflow separation locations.

1. Skin Friction

For the range of conditions mentioned in Sec. II.D, steady results over the axisymmetric model configuration show typical characteristics of the crossflow separation. Figure 5 shows the oil-flow visualization of the near-wall fluid over the constant-diameter region of the model and qualitatively describes the crossflow separation topology. Skin-friction lines converge along the separation lines. In Fig. 5, two separation lines can be identified on the leeward side of the model. The line closer to the windward side is defined as the *primary separation line* and the other as the *secondary separation line*.

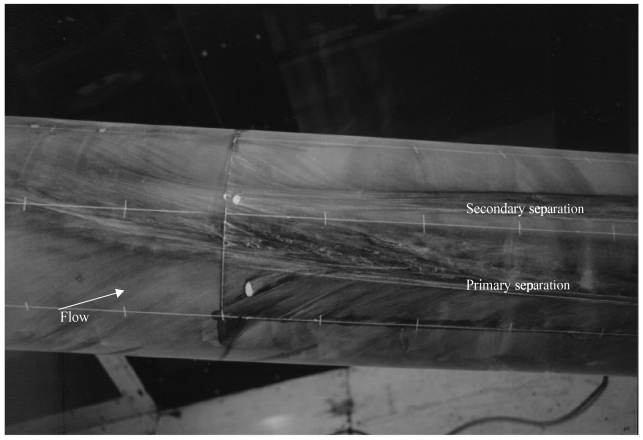

Fig. 5 Oil-flow visualization showing the crossflow separation topology on the constant-diameter region of the axisymmetric model at $\alpha = 20$ deg and $Re = 4.5 \times 10^6$; flow is from left to right.

To investigate the steady crossflow separation structure over the model, we first analyze the circumferential skin-friction behavior along the axial direction at a particular pitch angle. For that purpose, as a representative case, we show Fig. 6, which gives circumferential skin-friction C_f distribution for various axial (x/L) stations at a pitch angle of $\alpha = 15.3$ deg. At this pitch angle, $x/L = 0.266$ is the first station at which a minimum in the skin-friction distribution can be detected. This minimum indicates the primary separation location at a circumferential location of $\phi = 146$ deg. Starting from this station, the primary separation can be clearly seen as the first local minimum of the skin-friction distribution at all of the other axial stations downstream. The primary separation location moves toward the windward side as the flow travels downstream in the axial direction. It is also interesting to see the nearly flat profile at the vicinity of the minimum point for the last station ($x/L = 0.863$) located on the stern region. This profile indicates separated low-speed fluid in this complex flow region between $\phi \simeq 100$ and 130 deg, which makes the identification of the true minimum difficult.

The secondary separation location can be obtained by finding the second minimum in each circumferential skin-friction distribution. At this pitch angle, the secondary separation can be clearly observed starting from $x/L = 0.638$. As opposed to the primary separation line, the secondary separation location moves in the leeward direction as the flow particles travel downstream.

Another useful way of analyzing the crossflow separation is to examine the circumferential skin-friction distribution at various pitch angles at a particular axial location. Figure 7 shows the skin-friction distribution for all of the pitch angles covered in the steady measurements at the axial station $x/L = 0.501$. For this location, $\alpha = 7.2$ deg is the first pitch angle at which a primary separation was observed. With the further increase of the pitch angle, the primary separation location moves windward. The secondary separation can be identified starting from $\alpha = 15.3$ deg and moves leeward with increasing pitch angle. The measurements indicate that at a specific axial station, the primary separation location moves windward, whereas the secondary separation location shifts in the leeward direction as the pitch angle is increased.

2. Static Pressure

To determine the circumferential behavior of the mean pressure in the separated flow regions, steady pressure distributions are compared with the skin-friction variations at the same axial locations. Figure 8 shows this comparison at $x/L = 0.501$ and $\alpha = 21.4$ deg. A favorable pressure gradient was observed on the windward side of the model. The leeward side of the model can be thought of as a pressure-recovery region. However, due to the crossflow separation on the leeward side of the model, the general trend of the pressure coefficient does not follow a monotonic increase. The circumferential distribution of pressure is approximately constant over the separated fluid regions, which is a common characteristic in the vicinity of the separation locations. This flat pressure region extends over the primary and the secondary separation locations. As discussed by Wetzel et al. [6], although the pressure data are often used to indicate the existence of massive separation, they are not a good indicator for detecting the precise location of the crossflow separation. This is due to the fact that the crossflow separation is the result of local flow phenomena, but pressure at a given point in space is strongly influenced by the entire flowfield. One may also think to acquire unsteady pressure data to obtain force and moment information, however, the authors believe that large uncertainties associated with the inertial loads on the pressure transducers and the fine-spatial-resolution requirement for the integration of the pressures make this option less desirable.

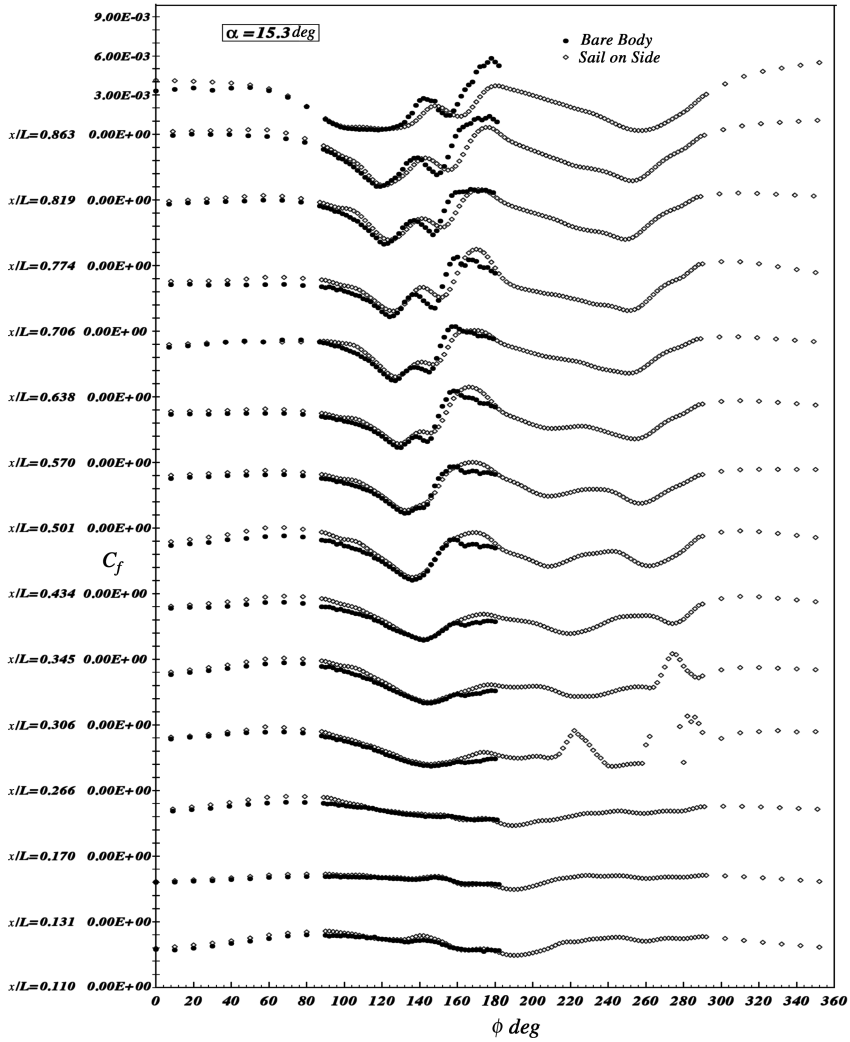

Fig. 6 Steady circumferential skin-friction distributions for all x/L locations for model bare-body and sail-on-side configurations; sail on side is on the right of the figure, starting from $\phi = 180$ deg (see Appendix B for the discussion on sail-on-side results).

B. Unsteady Results

1. *Unsteady Separation Topology*

One of the methods to investigate the difference between the steady and the unsteady flow separation over the model is to compare the steady circumferential skin-friction distribution obtained at a certain pitch angle α with the unsteady distribution acquired at the corresponding instantaneous pitch angle $\alpha(t')$. Figure 9 shows the steady primary and secondary separation locations and the unsteady primary separation locations at three angles of attack. Steady primary and secondary separation lines can be observed at $\alpha = 13.2$ deg, however, no separation is detected for the unsteady case at the corresponding instantaneous angle of attack. As the angle of attack is increased, the onset of an unsteady primary separation line can be seen, which is more leeward and downstream than the steady separation. No clear unsteady secondary separation can be detected even at the highest angle of attack covered in the experiments. Figure 8 shows the steady/unsteady circumferential skin-friction comparison at the axial station $x/L = 0.501$ and $\alpha = 21.4$ deg. The primary separation location for the steady data is $\phi = 122$ deg, whereas the unsteady primary separation occurs at $\phi = 138$ deg. The steady data have a secondary separation at $\phi = 148$ deg, whereas no secondary separation is observed for the unsteady case. The difference between the skin-friction magnitudes should also be noted; this difference is significant, especially in the leeward region between 150 and 180 deg, with steady values being higher than the unsteady values.

These results clearly show that the topology of the unsteady separation is different from the steady separation pattern. The difference originates from the fact that the unsteady separation location lags the steady separation. This can be clearly seen from Fig. 10, in which the quasi-steady and the unsteady primary separation locations are plotted against t' for different axial stations. In this figure, the horizontal distance between the unsteady and the steady separation location is an indication of the presence of a time lag. Because the maneuver was performed with a constant pitch rate, the instantaneous pitch angle is a linear function of t'. By considering this fact in examining Fig. 10, it can also be thought that at an instantaneous pitch angle, for a specific axial location, the unsteady separation starts more leeward than the steady case. This explains the cause of difference between the steady and the unsteady separation locations shown in Figs. 8 and 9.

One may also relate the nondimensional time leads between the steady and the unsteady forces measured on the same model geometry by Granlund and Simpson [8] to the unsteady-separation-location behavior described earlier. Time lags observed in the separation locations indicate the increase in attached circulation over the maneuvering body. This increase in the attached circulation creates greater force values than the steady case, and the unsteady force values lead the steady values.

2. *Time-Lag Models*

To understand why a lag exists, Wetzel and Simpson [4] suggested that one should examine the path of a fluid particle during the maneuver. During the pitch-up maneuver, a fluid particle originally starts its trajectory on the windward side of the model at a lower angle

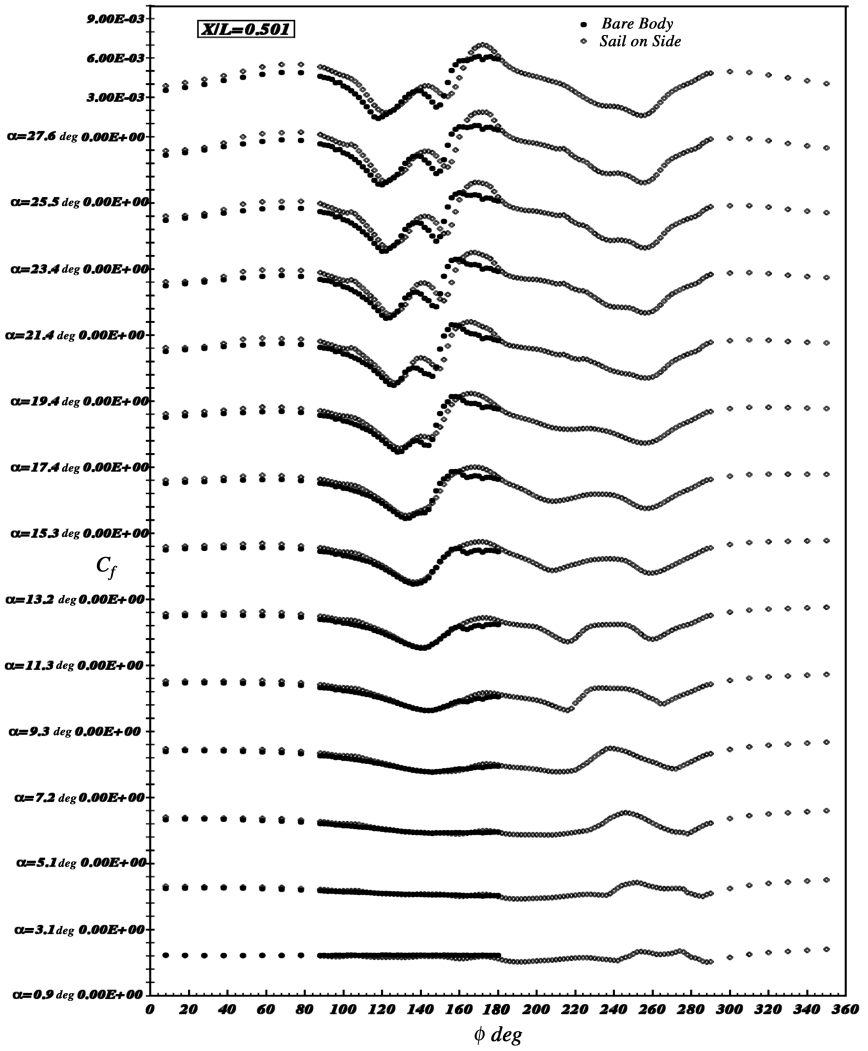

Fig. 7 Steady circumferential skin-friction distributions for all pitch angles for model bare-body and sail-on-side configurations; sail on side is on the right of the figure, starting from $\phi = 180$ deg (see Appendix B for the discussion on sail-on-side results).

of attack. Therefore, the particle experiences a less severe adverse-pressure gradient along its path and can travel farther around the leeside before separating, when compared with a similar particle in a steady flowfield. The main interest is to be able to develop physics-based models to approximate these time lags associated with the unsteady flowfields.

3. *Algebraic Time-Lag Models*

Algebraic time-lag modeling was a commonly used approach in the previous studies. Most of the algebraic time-lag models are based on finding an effective angle of attack α_{eff} by using the descriptions of the flow kinematics. If a model rotates about some point x_{cg} at a constant pitch rate $\dot{\alpha}$, a relative velocity normal to the model axis $\dot{\alpha}(x - x_{\text{cg}})$ will exist at other x/L locations, in addition to the velocity of the wind relative to the point of rotation. By using this fact, Montividas et al. [15] approximated an effective angle of attack as

$$\alpha_{\text{eff}} = \alpha - \Delta\alpha_{\text{eff}} \tag{2}$$

where

$$\Delta\alpha_{\text{eff}} = \dot{\alpha}\frac{x_{\text{cg}} - x}{U_\infty} \tag{3}$$

However, this approximation did not describe the unsteady effects in their flowfield associated with the onset of asymmetric vortex shedding at high angles of attack on ogive cylinders. Ericsson [16] also studied the same problem and extended the effective-angle-of-attack idea by including convective lag effects in the flowfield. He

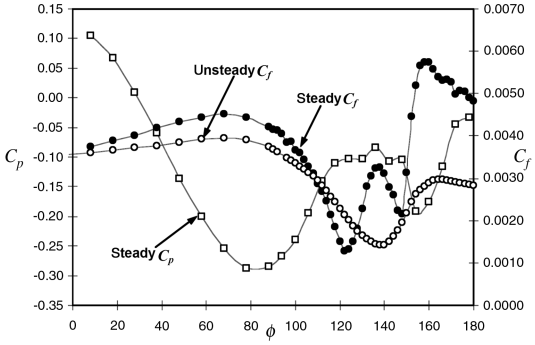

Fig. 8 Circumferential skin-friction (steady and unsteady) and pressure coefficient (steady) distributions at $\alpha = 21.4$ deg and $x/L = 0.501$ for the bare-body model configuration.

used the fact that a vortex at a downstream station of the apex of the model (ogive cylinder) will react to the changed flow conditions at the apex at a time Δt later. He also approximated that the disturbances originating at the apex of the model would propagate downstream with the freestream velocity, which would give $\Delta t = x/U_\infty$. By using this result in Eq. (3), Ericsson obtained

$$\Delta\alpha_{\text{eff}} = \dot{\alpha}\frac{x_{\text{cg}} + x}{U_\infty} \tag{4}$$

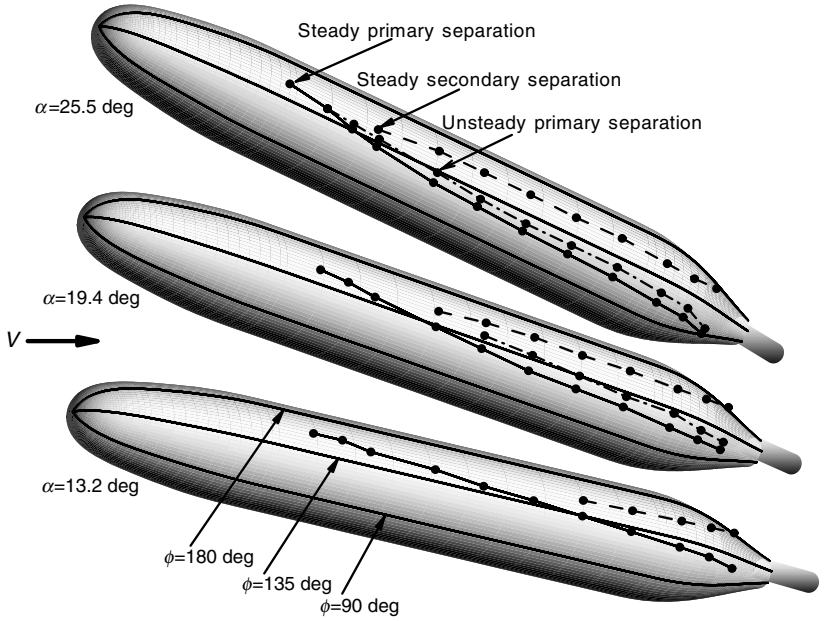

Fig. 9 Steady primary separation (solid line), steady secondary separation (dashed line), and unsteady primary separation (dotted-dashed line) lines at three angles of attack measured at the model center of rotation.

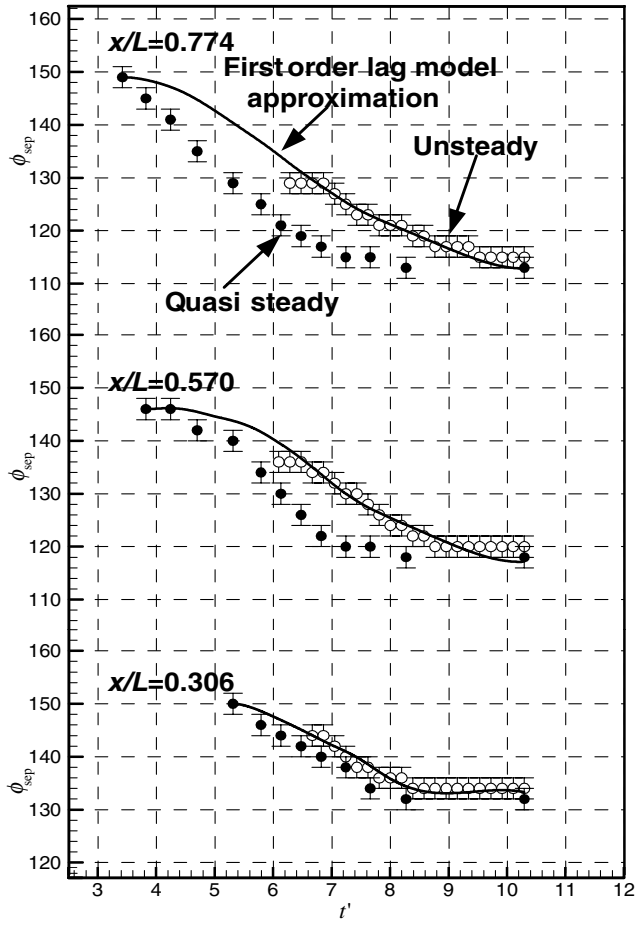

Fig. 10 Steady and unsteady primary separation locations along with the first-order differential time-lag approximation to the unsteady separation data; first-order time-lag approximation is computed by Eq. (5).

Equation (4) did successfully approximate the lags in asymmetric vortex shedding on the pitching ogive cylinder.

In our study, we calculated $\Delta\alpha_{\text{eff}}$ both from the experimental results and by using Eq. (4) at four different axial locations. Because

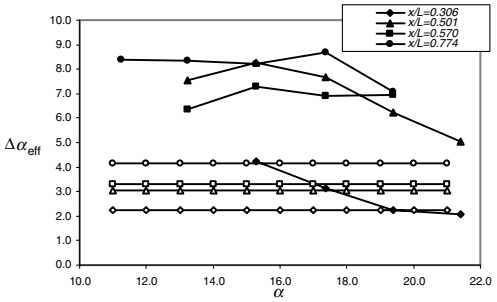

Fig. 11 Incremental effective angle of attack for the pitch-up maneuver at four x/L stations as a function of instantaneous angle of attack (DyPPiR pitch angle) α; open symbols show the effective angle of attack given by Eq. (4) (both angles are in degrees).

the pitch rate has a constant value of 78 deg/s, Eq. (4) gave constant $\Delta\alpha_{\text{eff}}$ values for each axial location. For calculating $\Delta\alpha_{\text{eff}}$ using experimental results, a certain number of unsteady separation locations ϕ_{sep} and corresponding instantaneous pitch angles $\alpha(t')$ were selected from the measured unsteady data. Then the same values for the steady separation locations and the corresponding steady pitch angles were picked. For a specific separation location, the difference between the instantaneous pitch angle and the steady pitch angle was calculated as the effective angle-of-attack increment. These values are compared with effective angle-of-attack increments obtained from Eq. (4) in Fig. 11. As can be seen from this figure, there is a significant difference between experimental $\Delta\alpha_{\text{eff}}$ and that calculated from Eq. (4), especially for the stations $x/L \geq 0.501$, for which the magnitudes of the experimental $\Delta\alpha_{\text{eff}}$ are twice as much higher than that obtained by using the model in Eq. (4). Also, although the pitch rate is constant, experimental $\Delta\alpha_{\text{eff}}$ does change with the instantaneous pitch angle and thus with the time. This comparison may indicate the difference between the time lags observed in the unsteady crossflow separation and those associated with the asymmetric vortex shedding on the ogive cylinder.

4. First-Order Differential Time-Lag Model

Goman and Khrabrov [17] developed a first-order time-lag model to approximate the time history of a dominant flow feature such as separation location in general unsteady flows. They applied this model to pitching two-dimensional airfoils, delta wings, and the

unsteady aerodynamics of a complex fighter-aircraft configuration. They used the separation location as an internal state variable and defined the forces and moments as functions of this state variable. For a given maneuver, by obtaining the time history of this state variable, they were able to calculate the unsteady force and moments. Wetzel and Simpson [4] implemented an extended version of this model for approximating the time-varying nature of the unsteady separation locations over the maneuvering prolate spheroid. The approximation successfully matched with the experimental unsteady separation locations, and nondimensional time-lag values for different axial stations were obtained. The same extended version of the first-order differential lag model was used in this study to approximate the unsteady primary separation locations over the bare-body model undergoing a pitch-up maneuver:

$$\tau'\left(\frac{x}{L}\right)\frac{\mathrm{d}\phi_{\mathrm{uns}}}{\mathrm{d}t'}+\phi_{\mathrm{uns}}\left(\frac{x}{L},t'\right)=\phi_0\left(\frac{x}{L},\alpha(t')\right) \tag{5}$$

In Eq. (5), ϕ_{uns} represents the approximation to the unsteady separation location, and ϕ_0 can be obtained from the steady separation data at each $\alpha=\alpha(t')$. Note that both ϕ_0 and ϕ_{uns} do also vary in the axial direction x/L. This is the difference between the extended version and the original time-lag model of Goman and Khrabrov [17]. In the original version, a single point of separation was considered. However, for the present study and the prolate-spheroid case, because the crossflow separation occurs along a line rather than a point (Fig. 9), ϕ_{uns} and ϕ_0 are also functions of x/L. It should also be noted that the time lag in Eq. (5) is taken as an unknown and is identified by fitting the model equation with the experimental data.

Equation (5) mainly correlates the unsteady separation locations to the quasi-steady data by the time lag. In the solution procedure, ϕ_0 was obtained by fitting a cubic spline to the steady data. The independent variable was t' in the fitting procedure. As the initial value for ϕ_{uns}, the first steady separation location in the steady data was used. For each axial station x/L, the model equation was solved with different values of the time lag in an iterative manner. The rms error between the approximated and experimental unsteady data was calculated at each iteration, and the τ' that gives the smallest error was chosen for each specific axial location. The details of the solution procedure can be found in [9]. Figure 10 shows the results of the time-lag model approximation to the unsteady data at $x/L=0.306$, 0.570, and 0.774, respectively. In these figures, the first-order lag-model approximation fits the measured unsteady separation locations reasonably well.

For each axial location, the nondimensional time-lag values obtained from the model equation fits are shown in Fig. 12. At the stations $x/L\le 0.266$, no unsteady separation location at any instant of time was observed. At the last station $x/L=0.863$, the determination of the unsteady separation location was not accurate enough, because of the flat nature of the circumferential skin-friction profile near the minimum, as discussed in the Steady Results section. In Fig. 12, near the model rotation point $x_{\mathrm{cg}}/L=0.24$, the time-lag value is close to zero, indicating that the quasi-steady data follow the unsteady data closely. An increase can be seen until the axial location $x/L=0.43$. Because there are not enough points in this region, the nature of this increase (linear or nonlinear) cannot be determined accurately. After this point, the time lag stays approximately constant between $x/L=0.43$ and $x/L=0.774$, taking an average value of 1.40. At $x/L=0.819$, this value drops to 1.24.

In the current study, the change in time lag along the axial direction is different from that observed in the prolate-spheroid study by Wetzel and Simpson [4]. In that case, which has the model center of rotation point at $x/L=0.5$, the increase in the time-lag value was almost linear over the length of the model, reaching a value of $\tau'=3.0$ at $x/L=0.8$. For the current study, the rotation point is at $x/L=0.24$, and the geometry is different from the prolate spheroid, having a relatively large length of a constant diameter before the model stern. Both of these factors may cause the difference observed between the two studies. One plausible explanation of the different time-lag trends may be the time required for the upstream boundary-layer vortical fluid to be convected around the body to displace inviscid fluid and form a leeside separation vortex structure with the same separation location as the steady case. One can observe this unsteady accumulation of vortical fluid in flow-visualization studies by Gad-el-Hak and Ho [18]. After the beginning of a transient motion, the separated flow region requires some time to be filled with vortical fluid. This hypothesis explains to some extent why the time lags in the prolate-spheroid case are so much larger at the same downstream x/L location than the SUBOFF results. For the prolate spheroid, the model diameter downstream of the point of rotation continuously decreases toward the tail. In nondimensional terms, a greater volume of vortical fluid must be convected and gathered to fill the leeside separation region than for the constant-diameter SUBOFF model. Because the SUBOFF model does have a constant-diameter region, the time lags within this region of this model length should be about the same, as is observed.

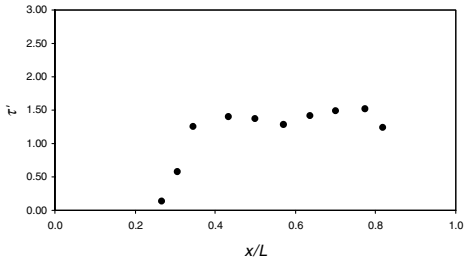

Fig. 12 Computed time lags at different x/L locations.

IV. Conclusions

This paper presents an experimental study on a maneuvering SUBOFF model, which was conducted to give detailed information on unsteady turbulent flow separation, to explain the difference between the steady and unsteady separation structure and to investigate algebraic and first-order differential time-lag models for approximating the unsteady flow separation locations. Both unsteady and steady results are presented for the bare-body (axisymmetric) configuration of the model, which can also be thought of as a missile or, to a certain extent, an aircraft-fuselage geometry. In the experiments, steady and unsteady skin-friction magnitudes were measured using calibrated hot-film sensors, each connected to a constant-temperature anemometer. The minimum of the circumferential skin-friction distribution at each axial-measurement station was used to locate the separation locations. The dynamic plunge-pitch-roll model mount is used to simulate a linear pitch-up maneuver, which is comparable to the dynamic motion of full-scale vehicles of interest, in terms of the nondimensional time.

The steady skin-friction measurements show that the flow on the leeward side of the model can be characterized by the crossflow separation. Significant time lags between unsteady and steady separation locations are observed, which produce the difference in separation topology. Time lags observed in the separation locations indicate the increase in attached circulation over the maneuvering SUBOFF model, which may explain why unsteady forces measured on similar geometries lead the steady values.

Algebraic time-lag models fail to give reasonable agreement with the experimental results, indicating the complex nature of the unsteady flow separation over the SUBOFF model or similar geometries that undergo high-excursion pitch-up maneuvers. A first-order differential time-lag model of Goman and Khrabrov [17] was shown to fit the unsteady data reasonably well. This model can be considered as a method of correlating the unsteady measurements to the quasi-steady data with a time lag. Using this model, the prediction of the unsteady flow characteristics from the steady data can be possible with the development of methods to estimate the time lags that vary based on the geometry used and maneuvers performed. In this study, the nondimensional time lags, which also vary as a function of the axial direction on the model surface, were obtained by fitting the model equation to the experimental data. The comparison

of current time-lag results to those of a previously performed experiment with a different model and point of rotation exhibits the difference in the time-lag magnitudes and in their spatial variation along the axial direction. The reason for different time lags between the two cases can be explained by the time duration required for the displacement of the leeside inviscid-fluid volume during a maneuver with vortical separated flow, which may vary for different geometries and points of rotation.

Appendix A: Calibration of the Hot-film Sensors

The hot-film sensors used in the experiments were calibrated on the constant-diameter section of the model with bare-body configuration at a 0-deg angle of attack to facilitate axisymmetric flow. Boundary-layer velocity profiles on the constant-diameter region of the model were taken at four calibration speeds: 24.4, 29, 33.5, and 42.7 m/s. Measurements for each speed were made at two stations: the first station was at the upstream location of the constant-diameter region ($x/L = 0.25$) and the second station was downstream ($x/L = 0.59$). By using the boundary-layer velocity profiles, the boundary-layer thickness, displacement thickness, momentum thickness, and the shape factor at each station were calculated by taking into account the transverse wall curvature effect, which was discussed by White [19]. The velocity measurements in the streamwise direction between these two stations also showed that the boundary-layer-edge velocity could be taken as constant along the constant-diameter region of the model. To determine the θ distribution between two measurement stations, the following momentum integral equation was used:

$$0.03138\left[Re_a \ell_n\left(1 + 9.337\frac{\theta}{a}\right)\right]^{-0.2857} = \frac{\mathrm{d}\theta}{\mathrm{d}x} \tag{A1}$$

This equation was obtained by using the approach used by Kays and Crawford [20] and by making necessary modifications to include the transverse curvature effects. Equation (A1), which represents an initial value problem, was solved numerically by using the modified Euler's method to determine the momentum-thickness distribution. As the initial value for the momentum thickness, the θ value measured at the second station was used. The experimental momentum-thickness value obtained for the boundary-layer velocity profile measured at the first station was compared with the value calculated from the solution of Eq. (A1) at the same location to verify the accuracy of method. After obtaining the momentum-thickness distribution, the skin-friction coefficient at each sensor location was determined using the Ludwieg–Tillmann equation:

$$\frac{C_f}{2} = 0.123 \times 10^{-0.678H}\left(\frac{U_e\theta}{\nu}\right)^{-0.268} \tag{A2}$$

The calibration C_f values were obtained for $1010 \le Re_\theta \le 4900$. For the calibration, the hot-film version of King's law was used:

$$\frac{E^2}{(T_w - T_\infty)} = A + B(\tau_w)^{1/3} \tag{A3}$$

where E is obtained from a hot-film sensor connected to a constant-temperature anemometer. The purpose of the calibration is to determine the coefficients A and B in Eq. (A3). For finding these coefficients, E and corresponding τ_w values obtained at the calibration speeds were used to make a linear regression. In Eq. (A3), the change in the freestream temperature will also cause a change in the calibration coefficients A and B. Because the temperature of the Virginia Tech Stability Wind Tunnel is ambient and cannot be controlled, the calibration procedure was repeated as the tunnel temperature changed. To minimize the uncertainty in the skin-friction measurements due to the freestream temperature change for the bare-body case, the calibration coefficients for each sensor were recalculated for every roll-angle position of the model before taking steady data and performing maneuver for that specific roll angle. The freestream temperature change was, at most, ± 0.5°C between each roll-angle position and this was included in the overall uncertainty calculations. For the measurements with the sail, calibration coefficients for each sensor were recalculated at approximately every 10 roll angles by simply detaching the sail from the body and applying the calibration procedure to the bare body.

Appendix B. Steady Sail-on-Side Skin-Friction Results

Steady skin-friction measurements of the sail-on-side case are compared with the bare-body results to emphasize the change in the separation structure. In Figs. 6 and 7, open symbols stand for the circumferential skin-friction distributions of the sail-on-side case. It is more appropriate to evaluate the results of the sail-on-side case in two separate regions: the region with no sail (between $\phi = 0$ and 180 deg) and the region with the sail (between $\phi = 180$ and 360 deg). In the first region, the origin and the variation of the primary and the secondary separation lines as a function of x/L and the pitch angle α show the same characteristics as defined for the bare-body case. This implies that the main flow feature on the nonsail region is the crossflow separation. Although the general trend is the same, in Fig. 6, for the stations $x/L \ge 0.501$ at $\alpha = 15.3$ deg, the locations of the primary and the secondary separations are slightly different from the bare-body separation locations: they are more leeward than the bare-body locations. The same difference can also be observed in Fig. 7 for $\alpha \ge 15.3$ deg at $x/L = 0.501$. Figure B1 shows the variation of the primary separation location with α for three different x/L stations. As can be seen from this figure, the primary separation locations of the bare-body case and the nonsail region of the sail-on-side case are approximately the same within uncertainties up to $\alpha = 15.3$ deg. Beyond this angle, the separation locations of the sail-on-side case start to deviate from the bare-body results having an offset in the leeward direction; this difference is obvious for $\alpha = 21.4$, 23.4, and 25.5 deg.

The flow structure on the sail side of the model is much different from that observed for the nonsail side. The flowfield in this region is strongly affected by the presence of the sail. In Fig. 6, in the sail region, a minimum can be located at four stations: $x/L = 0.306$, 0.345, 0.434, and 0.501 (corresponding ϕ locations are 224, 220, 212, and 210 deg), which may indicate a separation at these stations; however, for the rest of the stations downstream, this minimum vanishes. A second minimum in C_f can be seen at $x/L = 0.345$ and the rest of the stations downstream. This minimum has an approximately constant ϕ location of 256 ± 2 deg between $x/L = 0.501$ and the last station $x/L = 0.863$; the same trend can also be observed in Fig. 7. A minimum in C_f for $\alpha = 9.3$, 11.3, 13.2, and 15.3 deg at $\phi = 216$, 216, 208, and 208 deg, respectively, can be clearly located. The second minimum starts from $\alpha = 5.1$ deg and has a constant circumferential location of 256 ± 2 deg between $\alpha = 13.2$ and 27.6 deg. The results on the sail side indicate that the flowfield does differ from the crossflow separation structure observed for the bare-body and nonsail regions of the sail-on-side case. Therefore, the categorization of the separation locations as the

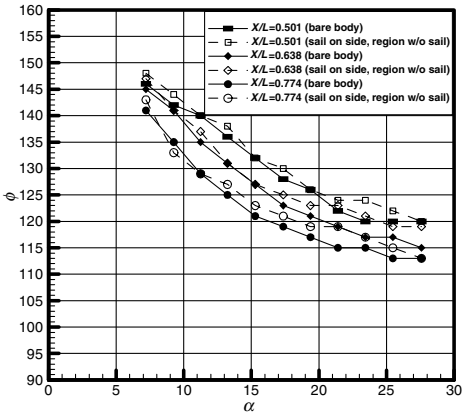

Fig. B1 Steady primary separation locations vs angle of attack for bare-body and sail-on-side cases.

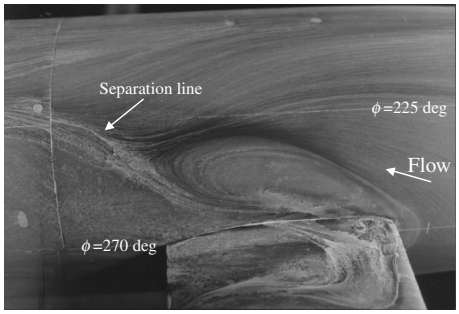

Fig. B2 Oil-flow pattern showing the separation in the vicinity of the sail at $\alpha = 15$ deg and $Re = 4.5 \times 10^6$; flow is from right to left.

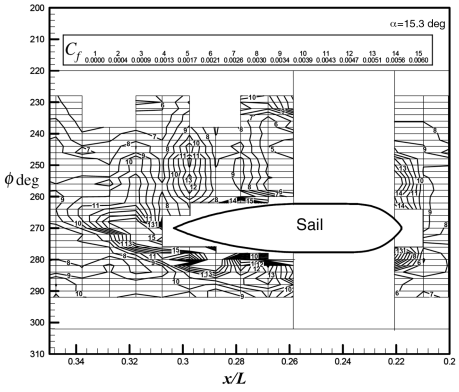

Fig. B3 Steady C_f contours in the vicinity of the sail.

primary or the secondary is not clear and may not reflect the real flow structure of this region. The flow in the vicinity of the sail-body junction is dominated by the horseshoe-type separation. This can be clearly seen from Fig. B2, which shows the oil-flow pattern in the leeward side of the sail region at $\alpha = 15$ deg. The separation line emanating from a three-dimensional stagnation point upstream of the sail extends from both the leeward and windward sides of the sail and travels downstream. The separation line on the leeward side of the sail can be seen along the converging skin-friction lines in Fig. B2. Although the flow topology near the onset of the horseshoe separation is different from that of the crossflow separation [21], both show similar characteristics of separated flows downstream: there is a strong convergence of the limiting streamlines on the surface and there are concentrated regions of vorticity in the flow, which may raise ambiguity about the identification of the separation pattern downstream of the sail. Figure B3 shows the C_f contours around the sail region at $\alpha = 15.3$ deg. Note that the blank areas are the regions in which no data were acquired. The vertical blank between $x/L \simeq 0.22$ and $x/L \simeq 0.26$ designates the ring area in which the sail is mounted. In this plot, a low-velocity region can be noticed at around $x/L = 0.27$ and $\phi = 245$ deg, which also matches with the oil-flow visualization results at that location. Skin-friction values on the hull take relatively large values at regions closer to the sail.

Acknowledgments

The present work was supported by the Office of Naval Research (ONR) grants N0014-96-1-0969 and N0014-99-1-0428, L. P. Purtell, Program Manager. The oil-flow visualizations were supplied by T. G. Wetzel. The experimental data are available on the Virginia Tech Department of Aerospace and Ocean Engineering website, http://www.aoe.vt.edu/~shosder/main/darpa2data/ [retrieved 29 Apr. 2007].

References

[1] Simpson, R. L., "Unsteady Aero-Hydrodynamics for Maneuvering Aircraft, Submarines and Automobiles," Dept. of Aerospace and Ocean Engineering, Virginia Polytechnic Inst. and State Univ., Rept. VPI-AOE-253, Blacksburge, VA, Nov. 1997.

[2] Simpson, R. L., "Some Experience with the Dynamic-Plunge-Pitch-Roll (DyPPiR) Mount in Unsteady Aerodynamics Research," 40th AIAA Aerospace Sciences Meeting, AIAA Paper 2002-0170, 2002.

[3] Wetzel, T. G., and Simpson, R. L., "Unsteady Flow over a 6:1 Prolate Spheroid," Dept. of Aerospace and Ocean Engineering, Virginia Polytechnic Inst. and State Univ., Rept. VPIAOE- 232, Blacksburg, VA, Defense Technical Information Center, Rept. ADA3071412XSP, Fort Belvoir, VA, 1996.

[4] Wetzel, T. G., and Simpson, R. L., "Unsteady Crossflow Separation Location Measurements on a Maneuvering 6:1 Prolate Spheroid," *AIAA Journal*, Vol. 36, No. 11, Nov. 1998, pp. 2063–2071.

[5] Etkin, B., *Dynamics of Atmospheric Flight*, Wiley, New York, 1972.

[6] Wetzel, T. G., Simpson, R. L., and Chesnakas, C. J., "Measurement of Three-Dimensional Crossflow Separation," *AIAA Journal*, Vol. 36, No. 4, Apr. 1998, pp. 557–564.

[7] Groves, N., Huang, T., and Chang, M., "Geometric Characteristics of DARPA SUBOFF Models," David Taylor Research Center, Report SHD-1298-01, Bethesda, MD, Mar. 1989; also Defense Technical Information Center (DTIC) *Public Scientific and Technical Information Network (STINET)* [online database], http://stinet.dtic.mil/ [retrieved 29 Apr. 2007].

[8] Granlund, K., and Simpson, R. L., "Unsteady Force and Moment Data on a Maneuvering Undersea Vehicle," AIAA Paper 2004-0729, 2004.

[9] Hosder, S., "Unsteady skin-friction Measurements on a Maneuvering DARPA2 SUBOFF Model," M.S. Thesis, Dept. of Aerospace and Ocean Engineering, Virginia Polytechnic Inst. and State Univ., Blacksburg, VA, June 2001; also available at http://scholar.lib.vt.edu/theses/available/etd-06152001-121441 [retrieved 29 Apr. 2007].

[10] Whitfield, C. C., "Steady and Unsteady Force and Moment Data on a Darpa2 Submarine," M.S. Thesis, Dept. of Aerospace and Ocean Engineering, Virginia Polytechnic Inst. and State Univ., Blacksburg, VA, July 1999; also available at http://scholar.lib.vt.edu/theses/available/etd-080399-173307 [retrieved 29 Apr. 2007].

[11] Wetzel, T. G., and Simpson, R. L., "Recent Steady and Unsteady Experiments for Submarine Fluid Dynamics: Unsteady Forces and Moments and Steady Oil Flow for the DARPA2," Dept. of Aerospace and Ocean Engineering, Virginia Polytechnic Inst. and State Univ., Rept. VPI-AOE 249, Blacksburg, VA, 1997.

[12] Simpson, R. L., Walker, D. A., and Shinpaugh, K. A., "Description of a 1000 Sensor Constant Current Anemometer System for Locating Three Dimensional Turbulent Boundary Layer Separations," Dept. of Aerospace and Ocean Engineering, Virginia Polytechnic Inst. and State Univ., Rept. VPI-AOE-185, Blacksburg, VA, Defense Technical Information Center, Rept. ADA2508273XSP, Fort Belvoir, VA, Dec. 1991.

[13] Miller, J. A., "A Simple Linearized Hot-Wire Anemometer," *Journal of Fluids Engineering*, Vol. 98, No. 3, 1976, pp. 550–557.

[14] Ahn, S., "An Experimental Study of Flow over a 6 to 1 Prolate Spheroid at Incidence," Ph.D. Thesis, Dept. of Aerospace and Ocean Engineering, Virginia Polytechnic Inst. and State Univ., Blacksburg, VA, Oct. 1992.

[15] Montividas, R. E., Reisenthel, P., and Nagib, H. N., "The scaling and Control of Vortex Geometry Behind Pitching Cylinders," AIAA Paper 89-1003, 1989.

[16] Ericsson, L. E., *Unsteady Flows in Tactical Missile Aerodynamics: General Topics*, edited by M. J. Hemsch, Progress in Astronautics and Aeronautics, AIAA, Washington, D.C., 1992, pp. 490–493.

[17] Goman, M., and Khrabrov, A., "State-Space Representation of Aerodynamic Characteristics of an Aircraft at High Angles of Attack," *Journal of Aircraft*, Vol. 31, No. 5, 1994, pp. 1109–1115.

[18] Gad-el Hak, M., and Ho, C. M., "Unsteady Flow Around an Ogive Cylinder," *Journal of Aircraft*, Vol. 23, No. 6, 1986, pp. 520–528.

[19] White, F. M., "An Analysis of Axissymmetric Turbulent Flow Past a Long Cylinder," *Journal of Basic Engineering*, Vol. 94, Mar. 1972, pp. 200–206.

[20] Kays, W. M., and Crawford, M. E., *Convective Heat and Mass Transfer*, McGraw–Hill, New York, 1980.

[21] Yates, L. A., and Chapman, G. T., "Streamlines, Vorticity Lines and Vortices Around Three Dimensional Bodies," *AIAA Journal*, Vol. 30, No. 7, July 1992, pp. 1819–1826.